

Intermediate field-induced phase of the honeycomb magnet $\text{BaCo}_2(\text{AsO}_4)_2$

Prashanta K. Mukharjee,^{1,*} Bin Shen,¹ Sebastian Erdmann,¹ Anton Jesche,¹ Julian Kaiser,¹
Priya R. Baral,² Oksana Zaharko,² Philipp Gegenwart,^{1,†} and Alexander A. Tsirlin^{3,‡}

¹*Experimental Physics VI, Center for Electronic Correlations and Magnetism,
Institute of Physics, University of Augsburg, 86159 Augsburg, Germany*

²*Laboratory for Neutron Scattering and Imaging (LNS),
Paul Scherrer Institute (PSI), CH-5232, Villigen, Switzerland*

³*Felix Bloch Institute for Solid-State Physics, University of Leipzig, 04103 Leipzig, Germany*
(Dated: March 8, 2024)

We use magnetometry, calorimetry, and high-resolution capacitive dilatometry, as well as single-crystal neutron diffraction to explore temperature-field phase diagram of the anisotropic honeycomb magnet $\text{BaCo}_2(\text{AsO}_4)_2$. Our data reveal four distinct ordered states observed for in-plane magnetic fields. Of particular interest is the narrow region between 0.51 and 0.55 T that separates the up-up-down order from the fully polarized state and coincides with the field range where signatures of the spin-liquid behavior have been reported. We show that magnetic Bragg peaks persist in this intermediate phase, thus ruling out its spin-liquid nature. However, the simultaneous nonmonotonic evolution of nuclear Bragg peaks suggests the involvement of the lattice, witnessed also in other regions of the phase diagram where large changes in the sample length are observed upon entering the magnetically ordered states. Our data highlight the importance of lattice effects in $\text{BaCo}_2(\text{AsO}_4)_2$.

Introduction. Quantum spin liquid (QSL) is an exotic state of matter in which strong quantum fluctuations prevent magnetic long-range order (LRO) down to very low temperatures [1]. The exactly solvable $S = \frac{1}{2}$ honeycomb Kitaev model possessing bond-dependent nearest-neighbor Ising-type interactions offers a promising venue for stabilizing the QSL ground state with the excitation spectrum described by emergent Majorana fermions and gauge fluxes [2]. Experimental realization of this model has been of significant interest. The d^5 (Ir^{4+} , Ru^{3+}) [3] and, more recently, d^7 (Co^{2+}) [4] transition-metal ions were proposed as suitable building blocks of the Kitaev magnets.

The majority of Ir-, Ru-, and Co-based honeycomb materials show long-range order in zero magnetic field [5, 6]. However, it was conjectured that they may lie in the vicinity of the QSL phase, and external field can be used to suppress long-range order, thus giving way to the spin liquid. Indeed, magnetic field applied along a suitable direction leads to a rapid suppression of the ordered phase in $\alpha\text{-RuCl}_3$ and $\beta\text{-Li}_2\text{IrO}_3$ above the critical fields of $B_c \simeq 7$ T and 2.8 T, respectively [7–9]. The behavior of $\alpha\text{-RuCl}_3$ above B_c remains vividly debated. Whereas quantized thermal Hall effect [10–12], oscillations in thermal conductivity [13–15], and a distinct excitation continuum [16, 17] observed in this field range might be vestiges of the spin-liquid behavior, no distinct phase associated with this putative spin liquid could be identified [18–21].

Here, we focus on the Co-based honeycomb magnet, $\text{BaCo}_2(\text{AsO}_4)_2$ (BCAO), that was recently proposed as a possible Kitaev candidate [22], and address its behavior right above B_c in the same region where putative signatures of the spin-liquid physics of $\alpha\text{-RuCl}_3$ have been revealed. The two materials show different sequences of

magnetically ordered states, double-zigzag-like and field-induced up-up-down (*uud*) orders in B CAO [23–25] vs. different types of zigzag order in $\alpha\text{-RuCl}_3$ [26]. Moreover, a detailed study of spin dynamics [27], along with *ab initio* calculations [28], suggested that an easy-plane $J_1 - J_3$ Hamiltonian is more suitable for B CAO than an extended Kitaev model commonly accepted for $\alpha\text{-RuCl}_3$ [5]. On the other hand, both materials show several apparent similarities. They can be polarized by moderate in-plane fields and demonstrate an unusual behavior right above B_c . The critical field of B CAO is as low as $B_c \simeq 0.5$ T. An excitation continuum [29] and a small linear contribution to the thermal conductivity [30], which is often associated with spinon excitations of the spin liquid, were recently reported in this field range, suggesting that B CAO might also be tuned toward a spin-liquid phase by the applied field.

In the following, we present the thermodynamic and microscopic characterization of B CAO with the special focus on the field range around B_c . Using several thermodynamic probes, we map out the temperature-field phase diagram of this material and uncover the previously overlooked intermediate phase that appears near B_c and separates the *uud* order from the fully polarized state. This intermediate phase coincides with the field range where both excitation continuum and linear-in-temperature thermal conductivity have been reported. However, it does not show characteristic signatures of a spin liquid, namely, the absence of the long-range magnetic order because the magnetic Bragg peak persists in this phase. The formation of such an intermediate phase is not compatible with the existing theories of B CAO. Its stabilization may involve lattice effects, which are also prominent in other regions of the phase diagram where our data evidence large changes in the sample length

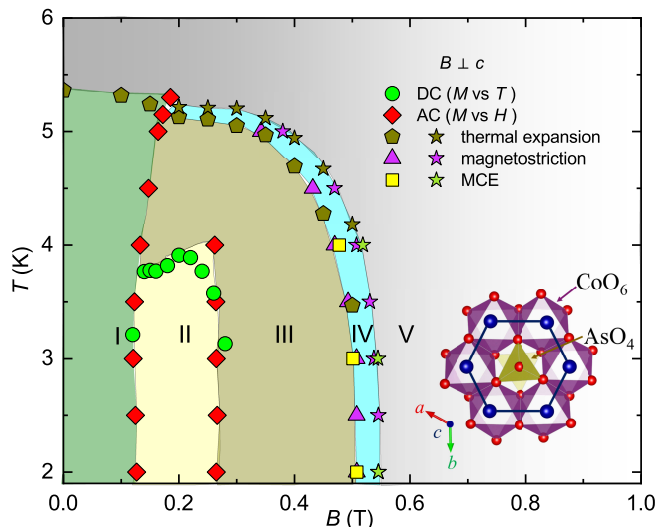


FIG. 1. Magnetic field-temperature (HT) phase diagram of $\text{BaCo}_2(\text{AsO}_4)_2$ for $B \perp c$ constructed from magnetization $M(T, B)$, dilatometry $L(T, B)$ and MCE measurements. Phase diagrams for different in-plane field directions are shown in Fig. S11. Inset: A honeycomb motif containing CoO_6 octahedra and AsO_4 tetrahedra at the center. The individual Co-honeycomb layers are stacked along the c -axis with Ba atoms separating them.

across several phase transitions.

Methods. Dark-pink-colored single crystals of BCAO were synthesized by the flux method [31]. High quality of these crystals was confirmed by an extensive mapping with Laue diffraction and by neutron diffraction (see Fig. S1). Temperature- and field-dependent magnetization was measured using the commercial SQUID magnetometer (MPMS3, Quantum Design), with orientation-dependent magnetization data collected using the sample rotation stage of MPMS3. Specific heat was measured using a standard relaxation technique in Quantum Design Physical Properties Measurement System (QD - PPMS). The magnetic Grüneisen parameter (Γ_m), which equals the adiabatic magnetocaloric effect (MCE), was determined by the alternating-field method [32]. Thermal expansion was measured with the aid of a compact ultrahigh-resolution capacitive dilatometer in the QD PPMS [33]. The length change as a function of temperature or field was recorded using a capacitance bridge (Andeen Haggerling 2550A). Neutron diffraction data from a single crystal were collected on the ZEBRA diffractometer at SINQ, Paul Scherrer Institute.

Phase diagram. Previous report revealed an almost isotropic behavior of BCAO within the honeycomb plane [27], in contrast to $\alpha\text{-RuCl}_3$ that showed different phase boundaries for two nonequivalent in-plane field directions, b and b^* [21, 26]. Our data for BCAO confirm this isotropic behavior. Therefore, in Fig. 1 we merged the data points obtained for different field directions,

whereas individual phase diagrams for $B \parallel b$ and $B \parallel b^*$ can be found in the Supplemental Material [Fig. S11]. In magnetometry, we determine temperature and field values from the peak positions of their respective derivatives. In dilatometry, we consider the peak positions of linear thermal expansion coefficient (α) and magnetostriction (λ), while in the MCE (Γ_m) data, we identify the transitions from the positions of the minima and zero-crossings [21].

Two magnetically ordered states of BCAO, the incommensurate double-zigzag order and commensurate uud order [23–25], are labeled as phases I and III in our phase diagram, respectively. Phase V is the fully polarized state. Additionally, we uncover phases II and IV that separate I from III and III from V, respectively. The main evidence for phase II comes from ac-susceptibility measurements, whereas phase IV is most crisply seen from dilatometry. This phase IV is of particular interest, as it at least partially coincides with the field range where signatures of the spin-liquid physics have been reported [29, 30].

Temperature-dependent dc-magnetization of BCAO [Fig. S2] shows an abrupt drop at T_N followed by a broad maximum that appears between 0.12 and 0.26 T, the field range that we identify as phase II. The boundaries of this phase are most clearly visible in the ac-susceptibility that shows two consecutive peaks as a function of field (Fig. 2a). The lower boundary of phase II is characterized by the abrupt increase in $M(B)$, suggesting that the transformation from the antiferromagnetic double-zigzag into the partially polarized uud state starts upon entering phase II. This transformation is first-order in nature, as witnessed by the large field hysteresis [Fig. S4]. The anomalies associated with phase II disappear around 4 K, whereas phases I and III survive up to 5.2 – 5.3 K.

The transition between I and III involves a flip of ferromagnetic zigzag spin chains from the $\uparrow\uparrow\downarrow\uparrow\uparrow\downarrow$ into the $\uparrow\uparrow\downarrow\uparrow\uparrow\downarrow$ configuration, which is essentially the creation and shift of domain walls. It is plausible that such a shift requires thermal energy and at lower temperatures involves an intermediate region, which we identify as phase II. This phenomenology may be similar to the isostructural $\text{BaCo}_2(\text{PO}_4)_2$ where magnetization curve shows distinct steps that correspond to discrete shifts of the domain walls, albeit at temperatures below 1 K only [34].

We now turn to thermal expansion (TE) and magnetostriction (MS) where all phase transitions are clearly visible thanks to the large lattice effects involved. BCAO shrinks along c upon entering phase I and expands along c upon entering phase III, but the most interesting behavior is seen in temperature-dependent thermal expansion measured above 0.2 T where sample length changes non-monotonically indicating two consecutive phase transitions, first with the decrease and then with the in-

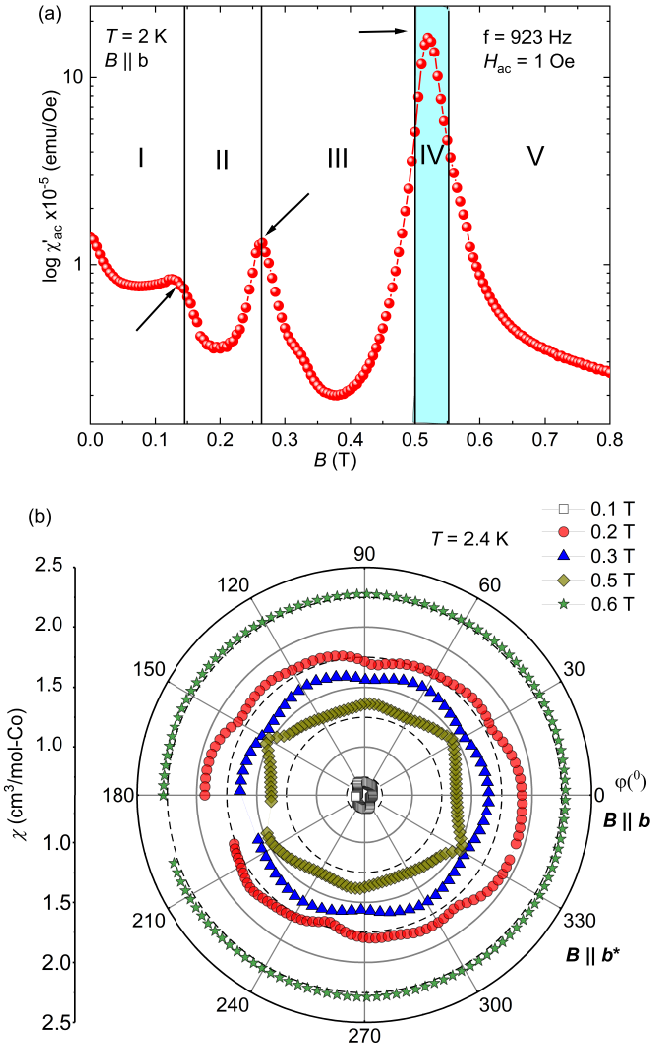


FIG. 2. (a) Magnetic field dependence of χ'_{ac} at 2 K for $B \parallel b$. The arrow marks indicate position of respective phase boundaries. (b) Angle-dependent magnetic susceptibility measured at $T = 2.4$ K, for different magnetic fields while rotating the crystal in the ab plane.

crease in c upon cooling (Fig. 3a). A similar behavior is seen in field-dependent sample length that changes non-monotonically on going from phase III into phase V (Fig. 3c). The two transitions can be tracked using the minima and maxima in linear thermal expansion coefficient $\alpha = (1/L_0)(d\Delta L/dT)$ and magnetostriction $\lambda = (1/L_0)(d\Delta L/dB)$ (Fig. 3b,d), resulting in the distinct region of phase IV that envelops phase III and separates it from phase V. This phase IV is remarkably different from phase II because it extends in temperature all the way up to 5.3 K where BCAO enters its paramagnetic state. Moreover, the transitions associated with phase IV should be second-order or weakly first-order in nature, as they do not show any significant hysteresis.

Intermediate phase. Phase IV is most clearly seen in the thermal expansion and magnetostriction

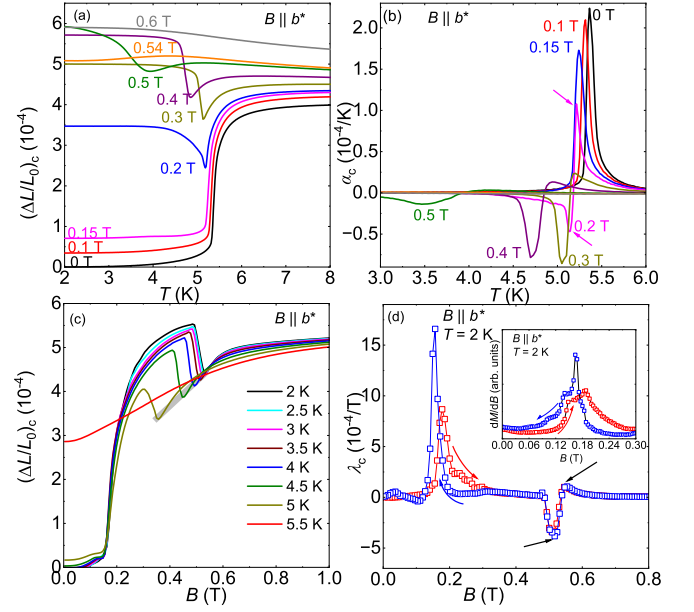


FIG. 3. Thermal expansion and magnetostriction plots of BCAO. (a) Normalized relative length changes vs temperature measured while warming at various fields. The curves are shifted vertically for clarity. (b) Plot of the linear TE coefficient (α) in different fields. For $B = 0$ T, in phase I, α shows a positive peak. As we move into phase II, α bifurcates to two peaks with opposite sign as indicated by the arrows. (c) Normalized relative length changes vs magnetic field measured while sweeping magnetic field up at several temperatures above and below T_N . The light grey line is a guide to eye showing the systematic shift of minimum around B_c . (d) Plot of linear MS coefficient λ vs. B at $T = 2$ K. Two prominent peaks are indicated by arrows around B_c . The transition around 0.15 T exhibits significant hysteresis, consistent with the field-dependent differential susceptibility [inset], reflecting its first-order nature.

data, whereas field-dependent dc-magnetization and ac-susceptibility merely show a broad peak around B_c , which is consistent with the presence of two consecutive transitions but does not prove the existence of an intermediate phase. This problem is at least partially mitigated in the MCE measurement where Γ_m displays the minimum and zero-crossing at the III–IV and IV–V boundaries, respectively [see Fig. S9]. It independently proves the existence of the intermediate phase. Additionally, we note that the symmetry of BCAO should change between phases III and IV. Fig. 2b shows angle-dependent susceptibility measured at different magnetic fields. While phase I is characterized by the quite low symmetry, phase III demonstrates the 6-fold symmetry expected for the ud state in the $R\bar{3}$ crystal structure. At 0.5 T, on approaching phase IV, the hexagon is turned by 30°, such that the minima and maxima of the susceptibility are swapped. It is also deformed [see Fig. S5b], indicating the loss of the 6-fold symmetry.

We further probed phase IV using neutron diffraction.

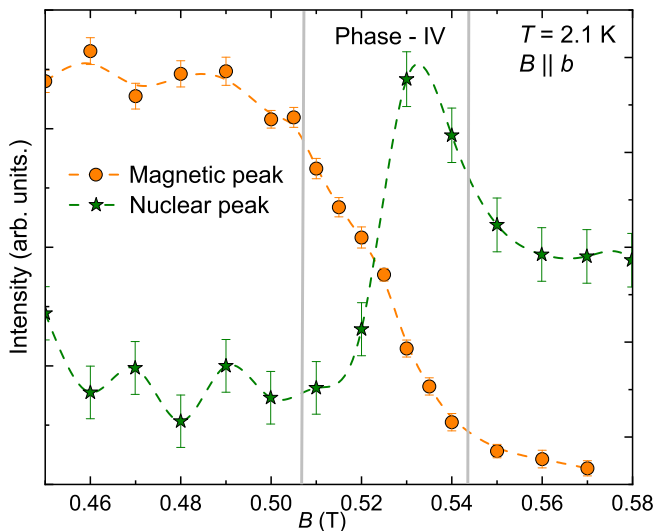


FIG. 4. Magnetic field dependence of magnetic and nuclear Bragg peak at $\mathbf{q} = (\frac{1}{3}, 0, -\frac{4}{3})$, and $(3, 0, 0)$ in phase IV for $B \parallel b$.

In phase III, we observed the magnetic Bragg peak at $\mathbf{q} = (\frac{1}{3}, 0, -\frac{4}{3})$ in agreement with the previous studies [24, 27]. This peak persists in phase IV but gradually loses its intensity and vanishes when the fully polarized state is reached [see Fig. 4]. At first glance, this behavior may suggest that phase IV is simply a two-phase region where the *uud* and fully polarized states coexist. In this case, one expects the gradual increase in the intensity of $\mathbf{q} = 0$ peaks through the shift of the magnetic intensity from $\mathbf{q} = (\frac{1}{3}, 0, -\frac{4}{3})$ to $\mathbf{q} = 0$ as magnetization increases. Some of the $\mathbf{q} = 0$ peaks indeed show abrupt changes around 0.51 and 0.55 T, but their intensity within phase IV changes non-monotonically as shown in Fig. 4. A lattice deformation may thus accompany the formation of phase IV, in agreement with the loss of the 6-fold symmetry in the angle-dependent susceptibility (see Fig. 2b). Field-induced intermediate phases stabilized by the spin-lattice coupling have been indeed reported in pyrochlore [35, 36] and triangular [37] magnets, albeit at much higher magnetic fields.

Pressure dependence of the transitions. BCAO shows remarkably large lattice effects upon its magnetic transitions. The zero-field transition toward phase I is accompanied by the relative length change of 4×10^{-4} , about four times larger than in α -RuCl₃ [20]. Despite such a strong coupling to the lattice, this transition appears as purely second-order, as it does not show any thermal hysteresis [Fig. S7]. The large lattice effects suggest that different phases of BCAO may be sensitive to pressure.

The peaks in α and λ yield the initial pressure dependence of the transitions. According to Maxwell's relation, $\lambda V = -(dM/dp)_{T,B}$ where V is the volume and M is the magnetization. Whereas we do not measure volume magnetostriction in our experiments, the quali-

tative behavior given by the positive ($\lambda_c > 0$) and negative peaks ($\lambda_c < 0$) in linear magnetostriction suggests that magnetization should decrease upon compression in phase I, whereas it should increase in phase III. The former trend is indeed confirmed by our isothermal magnetization measurements performed under hydrostatic pressure [Fig. S10c].

Pressure dependence of the transition temperature, dT_N/dp , is given by the Clausius-Clapeyron and Ehrenfest relations for the first- and second-order transitions, respectively. From the maxima and minima in α_c , we expect T_N to increase with pressure in phase I and decrease with pressure in phase III. These trends are again consistent with the direct magnetization measurements under hydrostatic pressure using both our data [31] and the earlier report [38]. Using the discontinuities of the volume thermal expansion coefficient and the specific heat measured in zero field, we obtain from the Ehrenfest relation $(dT_N/dp)_{p \rightarrow 0} \simeq 0.86$ K/GPa, which is several times larger than 0.3 K/GPa from our direct measurement of T_N under hydrostatic pressure [31]. This discrepancy probably indicates that the full pressure dependence of T_N up to 2 GPa deviates from the initial pressure dependence given by the ambient-pressure specific heat and thermal expansion. Indeed, the phase diagram of BCAO may drastically change under pressure because the $\frac{1}{3}$ -plateau indicative of the *uud* order is no longer seen at 1.6 GPa [31]. It means that phase III gives way to some other phase that allows a gradual increase in the magnetization, similar to phase IV at ambient pressure. Whether phase IV becomes the dominant field-induced state of BCAO under pressure would be an interesting question for further investigation.

Discussion. Our data reveal the previously overlooked aspect of BCAO, its narrow intermediate phase around B_c . A somewhat similar phase has been reported in α -RuCl₃ [21, 26] where maxima and minima of the angle-dependent susceptibility are also swapped upon entering this intermediate phase, around 6 T [26]. The intermediate phase of α -RuCl₃ has been understood as the change from the three-layer periodicity of zigzag order in low fields toward the six-layer periodicity as the result of anisotropic couplings between the layers [26]. Examining a similar scenario for BCAO is hindered by the broadness of its magnetic Bragg peaks along l [27], presumably due to the frustrated interlayer order. However, within the resolution of our measurement we observed neither the shift nor a change in the shape of the magnetic Bragg peak, which remains centered around $l \simeq -\frac{4}{3}$ across phase IV. The change in the interlayer order and the simple repetition of the α -RuCl₃ scenario in BCAO are thus unlikely.

Theoretical studies suggest that BCAO can be described by an easy-plane $J_1 - J_3$ model that hosts the double-zigzag ground state in zero field as a narrow region between the ferromagnetic and zigzag states [39–

41]. Assuming that BCO falls into this narrow region of the double-zigzag order, application of the magnetic field should produce the *uud* state followed by the fully polarized state, either directly or via a phase with canted V-type order [42]. However, this V-type order should be characterized by a different position of the magnetic Bragg peak in the *hk* plane compared to the *uud* state. Therefore, our data also rule out V-type order as the possible intermediate phase in this case.

The intermediate phase observed in our work does not cover the full field range where indications of the spin-liquid physics have been reported. Indeed, at least the linear-in-temperature contribution to the thermal conductivity extends up to 0.6 T [30], well into the fully polarized state. However, the onset of this unusual behavior at 0.50 T is clearly correlated with the formation of phase IV and not with reaching the fully polarized state around 0.55 T, so the presence of this intermediate phase must be taken into account when the microscopic scenario of the spin-liquid-like behavior of BCO is looked for.

Conclusions. Our comprehensive study of the anisotropic honeycomb magnet $\text{BaCo}_2(\text{AsO}_4)_2$ reveals an intermediate phase forming in this material near B_c , in the same field range where signatures of the spin-liquid behavior have been reported. While at first glance this behavior may look similar to the renowned $\alpha\text{-RuCl}_3$, our data suggest a different microscopic scenario. We show that signatures of the spin-liquid behavior observed in the field range near B_c should not be associated with the formation of a separate spin-liquid phase, because magnetic Bragg peaks persist throughout phase IV. Substantial lattice effects accompany the formation of this phase and should be important for understanding the intriguing physics of BCO.

We thank Pavel Maksimov, Sasha Chernyshev, Lukas Janssen, and Radu Coldea for fruitful discussions. P.K.M was supported by the Alexander von Humboldt foundation. The neutron single crystal diffraction experiment was performed at SINQ, Paul Scherrer Institute, Villigen, Switzerland. This work was funded by the Deutsche Forschungsgemeinschaft (DFG, German Research Foundation) – TRR 360 – 492547816.

[1] C. Broholm, R. J. Cava, S. A. Kivelson, D. G. Nocera, M. R. Norman, and T. Senthil, Quantum spin liquids, *Science* **367**, eaay0668 (2020).
 [2] A. Kitaev, Anyons in an exactly solved model and beyond, *Annals of Physics* **321**, 2 (2006).
 [3] G. Jackeli and G. Khaliullin, Mott insulators in the strong spin-orbit coupling limit: From Heisenberg to a quantum compass and Kitaev models, *Phys. Rev. Lett.* **102**, 017205 (2009).
 [4] H. Liu and G. Khaliullin, Pseudospin exchange interactions in d^7 cobalt compounds: Possible realization of the

Kitaev model, *Phys. Rev. B* **97**, 014407 (2018).
 [5] S. M. Winter, A. A. Tsirlin, M. Daghofer, J. van den Brink, Y. Singh, P. Gegenwart, and R. Valentí, Models and materials for generalized Kitaev magnetism, *J. Phys.: Condens. Matter* **29**, 493002 (2017).
 [6] C. Kim, H.-S. Kim, and J.-G. Park, Spin-orbital entangled state and realization of Kitaev physics in 3d cobalt compounds: a progress report, *J. Phys.: Condens. Matter* **34**, 023001 (2022).
 [7] H. Takagi, T. Takayama, G. Jackeli, G. Khaliullin, and S. E. Nagler, Concept and realization of Kitaev quantum spin liquids, *Nature Reviews Physics* **1**, 264 (2019).
 [8] A. Ruiz, A. Frano, N. P. Breznay, I. Kimchi, T. Helm, I. Oswald, J. Y. Chan, R. J. Birgeneau, Z. Islam, and J. G. Analytis, Correlated states in $\beta\text{-Li}_2\text{IrO}_3$ driven by applied magnetic fields, *Nature Comm.* **8**, 961 (2017).
 [9] M. Majumder, F. Freund, T. Dey, M. Prinz-Zwick, N. Büttgen, Y. Skourski, A. Jesche, A. Tsirlin, and P. Gegenwart, Anisotropic temperature-field phase diagram of single crystalline $\beta\text{-Li}_2\text{IrO}_3$: Magnetization, specific heat, and ^7Li NMR study, *Phys. Rev. Materials* **3**, 074408 (2019).
 [10] T. Yokoi, S. Ma, Y. Kasahara, S. Kasahara, T. Shibauchi, N. Kurita, H. Tanaka, J. Nasu, Y. Motome, C. Hickey, S. Trebst, and Y. Matsuda, Half-integer quantized anomalous thermal Hall effect in the Kitaev material candidate $\alpha\text{-RuCl}_3$, *Science* **373**, 568 (2021).
 [11] E. Lefrançois, G. Grissonnanche, J. Baglo, P. Lampen-Kelley, J.-Q. Yan, C. Balz, D. Mandrus, S. E. Nagler, S. Kim, Y.-J. Kim, N. Doiron-Leyraud, and L. Taillefer, Evidence of a phonon Hall effect in the Kitaev spin liquid candidate $\alpha\text{-RuCl}_3$, *Phys. Rev. X* **12**, 021025 (2022).
 [12] J. A. N. Bruin, R. R. Claus, Y. Matsumoto, N. Kurita, H. Tanaka, and H. Takagi, Robustness of the thermal Hall effect close to half-quantization in $\alpha\text{-RuCl}_3$, *Nature Phys.* **18**, 401 (2022).
 [13] P. Czajka, T. Gao, M. Hirschberger, P. Lampen-Kelley, A. Banerjee, J. Yan, D. G. Mandrus, S. E. Nagler, and N. P. Ong, Oscillations of the thermal conductivity in the spin-liquid state of $\alpha\text{-RuCl}_3$, *Nature Phys.* **17**, 915 (2021).
 [14] E. Lefrançois, J. Baglo, Q. Barthélemy, S. Kim, Y.-J. Kim, and L. Taillefer, Oscillations in the magnetothermal conductivity of $\alpha\text{-RuCl}_3$: Evidence of transition anomalies, *Phys. Rev. B* **107**, 064408 (2023).
 [15] J. A. N. Bruin, R. R. Claus, Y. Matsumoto, J. Nuss, S. Laha, B. V. Lotsch, N. Kurita, H. Tanaka, and H. Takagi, Origin of oscillatory structures in the magnetothermal conductivity of the putative Kitaev magnet $\alpha\text{-RuCl}_3$, *APL Materials* **10**, 090703 (2022).
 [16] A. Banerjee, P. Lampen-Kelley, J. Knolle, C. Balz, A. A. Aczel, B. Winn, Y. Liu, D. Pajerowski, J. Yan, C. A. Bridges, A. T. Savici, B. C. Chakoumakos, M. D. Lumsden, D. A. Tennant, R. Moessner, D. G. Mandrus, and S. E. Nagler, Excitations in the field-induced quantum spin liquid state of $\alpha\text{-RuCl}_3$, *npj Quantum Materials* **3**, 8 (2018).
 [17] A. Sahasrabudhe, M. A. Prosnikov, T. C. Koethe, P. Stein, V. Tsurkan, A. Loidl, M. Grüninger, H. Hedayat, and P. H. M. van Loosdrecht, Evidence for gapless quantum spin liquid in a honeycomb lattice, [arXiv:2305.03400](https://arxiv.org/abs/2305.03400).
 [18] S. Bachus, D. A. S. Kaib, Y. Tokiwa, A. Jesche, V. Tsurkan, A. Loidl, S. M. Winter, A. A. Tsir-

- lin, R. Valentí, and P. Gegenwart, Thermodynamic perspective on field-induced behavior of α -RuCl₃, *Phys. Rev. Lett.* **125**, 097203 (2020).
- [19] R. Schönemann, S. Imajo, F. Weickert, J. Yan, D. G. Mandrus, Y. Takano, E. L. Brosha, P. F. S. Rosa, S. E. Nagler, K. Kindo, and M. Jaime, Thermal and magnetoelastic properties of α -RuCl₃ in the field-induced low-temperature states, *Phys. Rev. B* **102**, 214432 (2020).
- [20] S. Gass, P. M. Cônsoli, V. Kocsis, L. T. Corredor, P. Lampen-Kelley, D. G. Mandrus, S. E. Nagler, L. Janssen, M. Vojta, B. Büchner, and A. U. B. Wolter, Field-induced transitions in the Kitaev material α -RuCl₃ probed by thermal expansion and magnetostriction, *Phys. Rev. B* **101**, 245158 (2020).
- [21] S. Bachus, D. A. S. Kaib, A. Jesche, V. Tsurkan, A. Loidl, S. M. Winter, A. A. Tsirlin, R. Valentí, and P. Gegenwart, Angle-dependent thermodynamics of α -RuCl₃, *Phys. Rev. B* **103**, 054440 (2021).
- [22] R. Zhong, T. Gao, N. P. Ong, and R. J. Cava, Weak-field induced nonmagnetic state in a Co-based honeycomb, *Sci. Adv.* **6**, eaay6953 (2020).
- [23] L. Regnault, P. Burlet, and J. Rossat-Mignod, Magnetic ordering in a planar XY model: BaCo₂(AsO₄)₂, *Physica B+C* **86-88**, 660 (1977).
- [24] L. P. Regnault and J. Rossat-Mignod, Effect of a magnetic field on the magnetic ordering of BaCo₂(AsO₄)₂, *J. Magn. Magn. Mater.* **14**, 194 (1979).
- [25] L.-P. Regnault, C. Boullier, and J. Lorenzo, Polarized-neutron investigation of magnetic ordering and spin dynamics in BaCo₂(AsO₄)₂ frustrated honeycomb-lattice magnet, *Heliyon* **4**, e00507 (2018).
- [26] C. Balz, L. Janssen, P. Lampen-Kelley, A. Banerjee, Y. H. Liu, J.-Q. Yan, D. G. Mandrus, M. Vojta, and S. E. Nagler, Field-induced intermediate ordered phase and anisotropic interlayer interactions in α -RuCl₃, *Phys. Rev. B* **103**, 174417 (2021).
- [27] T. Halloran, F. Desrochers, E. Z. Zhang, T. Chen, L. E. Chern, Z. Xu, B. Winn, M. Graves-Brook, M. B. Stone, A. I. Kolesnikov, Y. Qiu, R. Zhong, R. Cava, Y. B. Kim, and C. Broholm, Geometrical frustration versus Kitaev interactions in BaCo₂(AsO₄)₂, *Proc. Nat. Acad. Sci.* **120**, e2215509119 (2023).
- [28] P. A. Maksimov, A. V. Ushakov, Z. V. Pchelkina, Y. Li, S. M. Winter, and S. V. Streltsov, Ab initio guided minimal model for the "Kitaev" material BaCo₂(AsO₄)₂: Importance of direct hopping, third-neighbor exchange, and quantum fluctuations, *Phys. Rev. B* **106**, 165131 (2022).
- [29] X. Zhang, Y. Xu, T. Halloran, R. Zhong, C. Broholm, R. J. Cava, N. Drichko, and N. P. Armitage, A magnetic continuum in the cobalt-based honeycomb magnet BaCo₂(AsO₄)₂, *Nat. Mater.* **22**, 58 (2023).
- [30] C. Tu, D. Dai, X. Zhang, C. Zhao, X. Jin, B. Gao, T. Chen, P. Dai, and S. Li, Evidence for gapless quantum spin liquid in a honeycomb lattice, [arXiv:2212.07322](https://arxiv.org/abs/2212.07322).
- [31] See Supplemental Material for details of the experimental methods and sample characterization, as well as phase diagrams for different in-plane field directions.
- [32] Y. Tokiwa and P. Gegenwart, High-resolution alternating-field technique to determine the magnetocaloric effect of metals down to very low temperatures, *Rev. Sci. Instrum.* **82**, 013905 (2011).
- [33] R. KÜchler, A. Wörl, P. Gegenwart, M. Berben, B. Bryant, and S. Wiedmann, The world's smallest capacitive dilatometer, for high-resolution thermal expansion and magnetostriction in high magnetic fields, *Rev. Sci. Instrum.* **88**, 083903 (2017).
- [34] X. Wang, R. Sharma, P. Becker, L. Bohatý, and T. Lorenz, Single-crystal study of the honeycomb XXZ magnet BaCo₂(PO₄)₂ in magnetic fields, *Phys. Rev. Materials* **7**, 024402 (2023).
- [35] A. Miyata, H. Suwa, T. Nomura, L. Prodan, V. Fellea, Y. Skourski, J. Deisenhofer, H.-A. K. von Nidda, O. Portugall, S. Zherlitsyn, V. Tsurkan, J. Wosnitzer, and A. Loidl, Spin-lattice coupling in a ferrimagnetic spinel: Exotic $H - T$ phase diagram of MnCr₂S₄ up to 110 T, *Phys. Rev. B* **101**, 054432 (2020).
- [36] M. Gen, A. Ikeda, K. Aoyama, H. O. Jeschke, Y. Ishii, H. Ishikawa, T. Yajima, Y. Okamoto, X. Zhou, D. Nakamura, S. Takeyama, K. Kindo, Y. H. Matsuda, and Y. Kohama, Signatures of a magnetic superstructure phase induced by ultrahigh magnetic fields in a breathing pyrochlore antiferromagnet, *Proc. Nat. Acad. Sci.* **120**, e2302756120 (2023).
- [37] T. Nakajima, N. Terada, S. Mitsuda, and R. Bewley, Spin-driven bond order in a 1/5-magnetization plateau phase in the triangular lattice antiferromagnet CuFeO₂, *Phys. Rev. B* **88**, 134414 (2013).
- [38] S. Huyan, J. Schmidt, E. Gati, R. Zhong, R. J. Cava, P. C. Canfield, and S. L. Bud'ko, Hydrostatic pressure effect on the Co-based honeycomb magnet BaCo₂(AsO₄)₂, *Phys. Rev. B* **105**, 184431 (2022).
- [39] S. Jiang, S. R. White, and A. L. Chernyshev, Quantum phases in the honeycomb-lattice $J_1 - J_3$ ferro-antiferromagnetic model, *Phys. Rev. B* **108**, L180406 (2023).
- [40] A. Bose, M. Routh, S. Voleti, S. K. Saha, M. Kumar, T. Saha-Dasgupta, and A. Paramakanti, Proximate Dirac spin liquid in the honeycomb lattice $J_1 - J_3$ XXZ model: Numerical study and application to cobaltates, *Phys. Rev. B* **108**, 174422 (2023).
- [41] Y. Watanabe, S. Trebst, and C. Hickey, Frustrated ferromagnetism of honeycomb cobaltates: Incommensurate spirals, quantum disordered phases, and out-of-plane Ising order, [arXiv:2212.14053](https://arxiv.org/abs/2212.14053).
- [42] P. A. Maksimov, Proximity-induced sequence of field transitions in the Kitaev candidate BaCo₂(AsO₄)₂, *Phys. Rev. B* **108**, L180405 (2023).
- [43] J.-Q. Yan, S. Okamoto, Y. Wu, Q. Zheng, H. D. Zhou, H. B. Cao, and M. A. McGuire, Magnetic order in single crystals of Na₃Co₂SbO₆ with a honeycomb arrangement of 3d⁷ Co²⁺ ions, *Phys. Rev. Mater.* **3**, 074405 (2019).
- [44] R. D. Johnson, S. C. Williams, A. A. Haghighirad, J. Singleton, V. Zapf, P. Manuel, I. I. Mazin, Y. Li, H. O. Jeschke, R. Valentí, and R. Coldea, Monoclinic crystal structure of α -RuCl₃ and the zigzag antiferromagnetic ground state, *Phys. Rev. B* **92**, 235119 (2015).
- [45] J. Rodríguez-Carvajal, Recent advances in magnetic structure determination by neutron powder diffraction, *Physica B: Condens. Matter* **192**, 55 (1993).
- [46] B. Shen, A. Jesche, M. L. Seidler, F. Freund, P. Gegenwart, and A. A. Tsirlin, Interplay of magnetism and dimerization in the pressurized kitaev material β -Li₂IrO₃, *Phys. Rev. B* **104**, 134426 (2021).

Supplementary Material for Intermediate field-induced phase of the honeycomb magnet $\text{BaCo}_2(\text{AsO}_4)_2$

CRYSTAL GROWTH

Single crystals of $\text{BaCo}_2(\text{AsO}_4)_2$ were grown by a similar method as reported in [S22]. Dark-pink, hexagonal plate-like crystals (inset of Fig. S1a) were separated from the flux by washing in hot water. A few crystals were crushed into powders, and room-temperature powder XRD data were collected. To determine the sample orientation and possible stacking disorder, we collected X-ray Laue back reflection patterns (Photonic Sciences) (Fig. S1b). The clear Laue spots indicate the high quality of the BCO single crystal. In contrast to findings in other honeycomb materials [S43], our Laue pattern clearly shows the absence of rod-like diffuse spots, effectively ruling out the presence of defects/stacking faults in BCO. Moreover, through extensive Laue photography covering the entirety of the crystal surface, we have confirmed that BCO crystals exhibit a monodomain structure, contrasting with the multi-domain structure, which is often observed in $\alpha\text{-RuCl}_3$ [S44].

A few crystals were crushed into fine powder, and room-temperature x-ray diffraction data were recorded using the Empyrean powder diffractometer from PANalytical ($\text{CuK}\alpha$ radiation, $\lambda_{\text{avg}} \simeq 1.5418 \text{ \AA}$). Rietveld refinement for the collected data performed using the "FULLPROF" software [S45] confirms the single phase of BCO and returns lattice constants of $a = 5.0052(2) \text{ \AA}$ and $c = 23.481(1) \text{ \AA}$, which are consistent with the previous report [S22].

MAGNETIZATION AND SPECIFIC HEAT

The evolution of T_N was tracked from the magnetic susceptibility measured in different applied magnetic fields for the $B \parallel b$ orientation as shown in Fig. S2(a). In Fig. S2(b), we show a broad hump around 3.2 K, observed in the field range of 0.12 to 0.26 T and associated with phase II in the phase diagram. The transition at $T_N \simeq 5.35 \text{ K}$ decreases systematically before completely vanishing at $\sim 0.55 \text{ T}$. Magnetic isotherms collected for $5.5 \text{ K} \leq T \leq 2 \text{ K}$ are shown in Fig. S2(c). To estimate the magnetic couplings between the Co^{2+} ions, we have performed Curie-Weiss (CW) fit of the susceptibility data using $\chi = \chi_0 + C/(T - \theta)$, where χ_0 is the temperature-independent contribution, C is the Curie constant, θ is the CW temperature. The fit in the region 150 – 300 K yields a positive CW temperature $\theta_{\parallel,b} \simeq 37 \text{ K}$ suggesting predominant ferromagnetic interactions. From the obtained value of C , the effective paramagnetic moment (μ_{eff}) is estimated to be $\mu_{\text{eff},\parallel,b} \simeq 5.58\mu_B$ [see Fig. S2(d)]. These estimations are in agreement with the literature [S22, S30]. The deviation of the obtained effective moment (taking $= g\sqrt{J(J+1)}$, where g is the Landé g -factor and $J = 1/2$) from the theoretical value for spin- $\frac{1}{2}$ ($1.73 \mu_B$) arises due to the significant spin-orbit coupling, which is common in Co^{2+} quantum magnets.

The second-order nature of the transition into phase I is supported by examining the T -dependent susceptibility (at 0.01 T) throughout field-cooled-cooling (FCC) and field-cooled-warming (FCW) processes [see Fig. S2(e)]. The curves for both directions are reversible with no hysteresis. We have also measured temperature-dependent specific heat for $B \parallel a^*$ as shown in Fig. S2(f). In zero-field, $C_p(T)$ shows a sharp peak at T_N , which gradually decreases with increasing magnetic field and vanishes above 0.5 T, in line with other experiments.

DILATOMETRY

High-resolution capacitive dilatometry was used to measure length changes $L(T, H)$. The experimental design is described in Ref. [S33]. In all our experiments, we measured the relative length changes along the c -direction, while for field-dependent measurements, the magnetic field was oriented along the b and b^* -direction. The normalized relative length change is defined as follows,

$$\frac{\Delta L(T, B)}{L_0} = \frac{L(T, B) - L(300 \text{ K}, 0 \text{ T})}{L(300 \text{ K}, 0 \text{ T})}. \quad (\text{S1})$$

Here, L_0 is the sample thickness at 300 K and 0 T. Throughout our analysis, $\Delta L(T, B)$ values are standardized to the value at 2 K and 0 T. For thermal expansion, the data were collected during cooling-warming cycles with the sweep rate of 0.2 K/min. Magnetostriction measurements were performed up to 1 T with the sweep rate of 60 mT/min. To

calculate the pressure dependence of T_N , we use the Ehrenfest relation for a second-order transition,

$$\frac{dT_N}{dp} = V_m T_N \frac{\Delta\beta}{\Delta C_p} \quad (\text{S2})$$

where $V_m = 2.54 \times 10^{-5} \text{ m}^3/\text{mol}$ is the molar volume, $\Delta\beta = \Delta\alpha_{a^*} + \Delta\alpha_b + \Delta\alpha_c$ is the jump in the volume thermal expansion coefficient at T_N , and ΔC_p is the jump in C_p at T_N . For this purpose a crystal was cut into a rectangular shape and corresponding thermal expansion and specific heat are measured as shown in Fig. S6.

Figure S8(a) depicts the magnetostriction and field-dependent differential susceptibility (dM/dB) together for $T = 2 \text{ K}$. The first-order transformation (phase I \leftrightarrow phase II) is evidenced by a sharp peak both in λ_c and dM/dB plots. Near B_c (in phase IV), λ_c shows two peaks, whereas dM/dB features a broad behavior. Figure S8(b) shows the variation of λ_c with magnetic fields for $5.5 \text{ K} \leq T \leq 2 \text{ K}$.

MAGNETOCALORIC EFFECT

Field dependence of the magnetic Grüneisen parameter (Γ_m) is used to track field-induced states around B_c . This is done via the magnetocaloric effect (MCE) measurement under quasiadiabatic conditions. The magnetic Grüneisen parameter is defined as

$$\Gamma_m = \frac{1}{T} \frac{\partial T}{\partial B}. \quad (\text{S3})$$

This method utilizes the alternating-field technique [S32], wherein a weakly oscillating magnetic field with an amplitude (ΔB) is applied. This induces oscillations in the sample temperature (ΔT) due to the MCE. In this method, the heat-capacity setup is directly employed, enabling simultaneous measurement of both heat capacity and the Grüneisen parameter. The variations of Γ_m vs. B for three temperatures are shown in Fig. S9.

PRESSURE-DEPENDENT MAGNETIZATION

Magnetization studies under pressure were performed in the QD MPMS SQUID magnetometer. A single crystal of BCO was loaded into the CuBe cell. Pressure was determined by measuring the superconducting transition of a small piece of Pb. Daphne oil was used as a pressure transmitting medium. The details of the experimental procedure can be found in [S46].

SINGLE CRYSTAL NEUTRON DIFFRACTION

Single-crystal neutron diffraction was performed on the neutron diffractometer ZEBRA at SINQ, PSI. The crystal of the size $3 \times 3 \times 0.3 \text{ mm}^3$ was mounted into the 10 T vertical magnet with the b -axis vertical. Neutrons of the wavelength 1.383 \AA selected by the Ge-monochromator were used in the normal beam geometry.

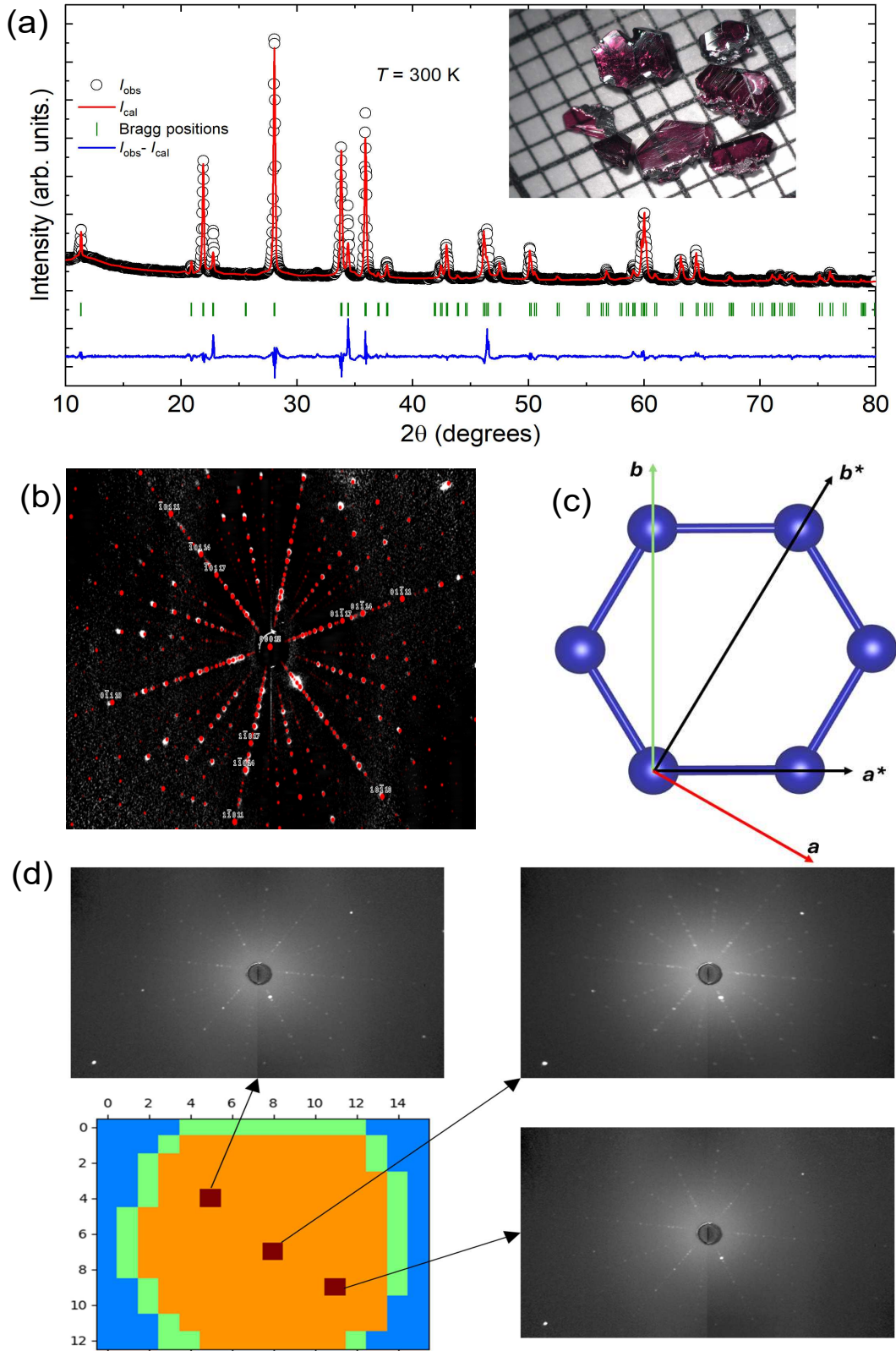


FIG. S1. (a) Powder x-ray diffraction data for $\text{BaCo}_2(\text{AsO}_4)_2$ collected at $T = 300 \text{ K}$ (black circles). The red lines indicate the Rietveld refinement fit of the data. The Bragg peaks are denoted by green vertical bars and the bottom blue line denotes the difference between the experimental and calculated intensities. Inset: Dark pink crystals on a millimeter paper. (b) Laue pattern of a crystal taken from the c -direction. The red spots represent simulated Laue patterns generated using Crystal Maker software. (c) A Schematic sketch of the convention used for different crystallographic orientations. (d) Laue back-scattering grid analysis was utilized to map out possible domains in the single crystal of BCO. The diffraction images were color-coded: orange for good diffraction images, green for weak patterns (edges), and blue for no observable patterns (sample holder). It was confirmed that different spots on the crystal surface had the same crystallographic orientation, thus excluding multi-domain growth.

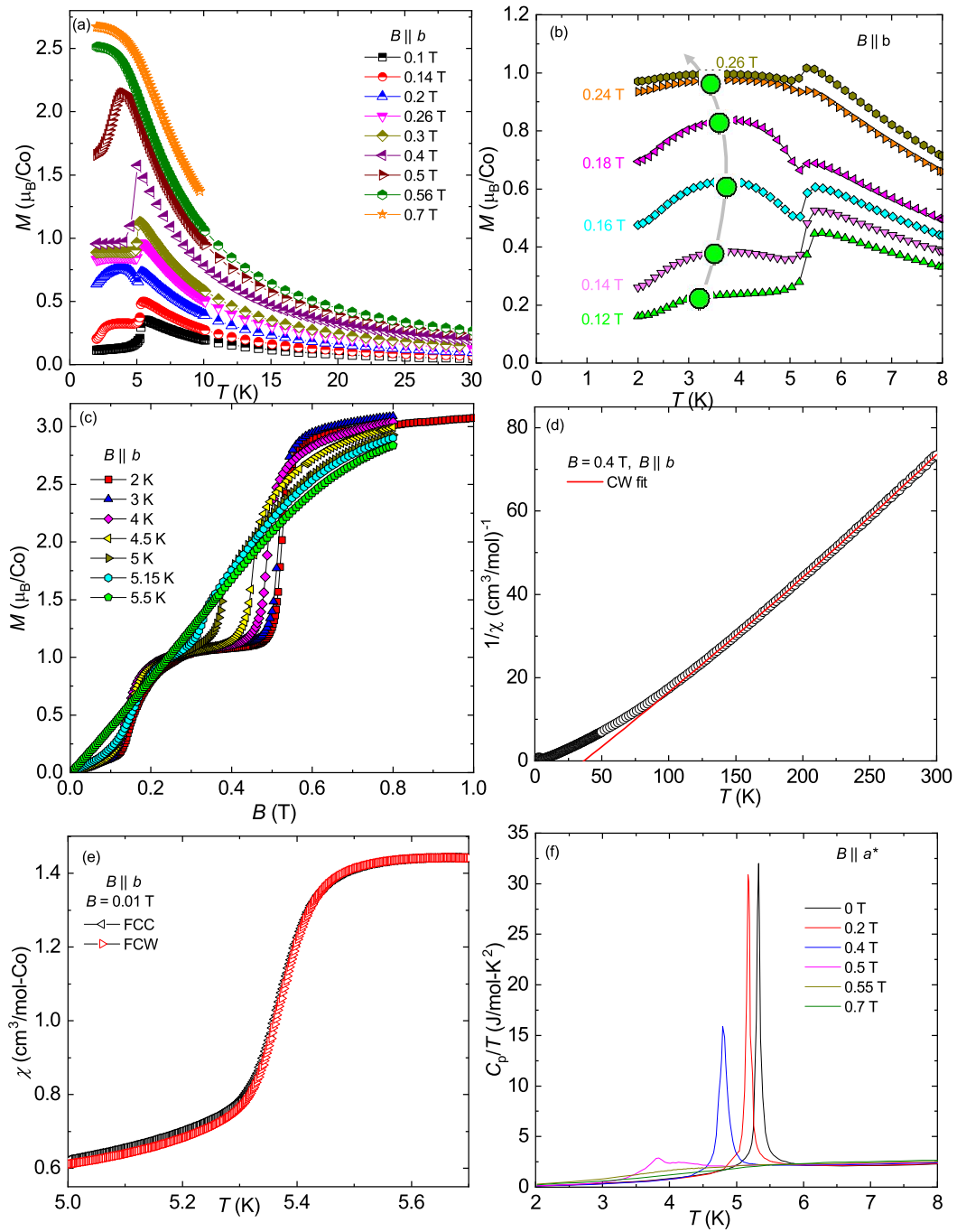


FIG. S2. (a) Magnetic susceptibility vs. temperature under magnetic fields up to 0.7 T. (b) $\chi(T)$ measured for $0.12 \text{ T} \leq B \leq 0.26 \text{ T}$ where a broad hump has been observed. The green circles indicate the corresponding broad maximum positions. (c) Magnetic isotherms measured for $5.5 \text{ K} \leq T \leq 2 \text{ K}$. (d) Inverse susceptibility vs. temperature along with the CW fit (red solid line). (e) $\chi(T)$ measured at $B = 0.01 \text{ T}$ for FCC-FCW cycle. (f) Specific-heat divided by temperature [C_p/T] vs. T for $0 \text{ T} \leq H \leq 0.7 \text{ T}$.

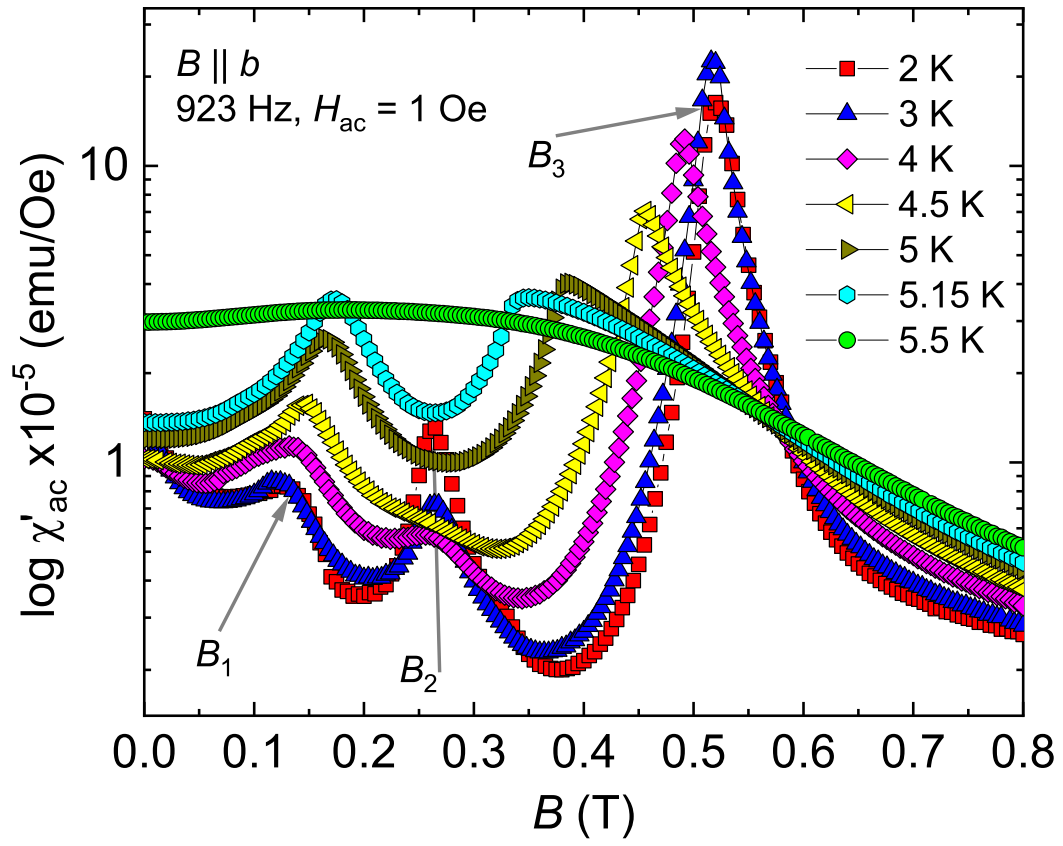


FIG. S3. Magnetic field dependence of χ'_{ac} for $5.5 \text{ K} \leq T \leq 2 \text{ K}$ for $B \parallel b$. Three clear transitions marked as B_1 , B_2 , and B_3 are observed at 2 K. As temperature increases up to T_N : B_1 initially remains constant, then steadily increases, B_2 remains stable until 4 K, then abruptly disappears above this, B_3 exhibits a consistent decrease beyond 3 K.

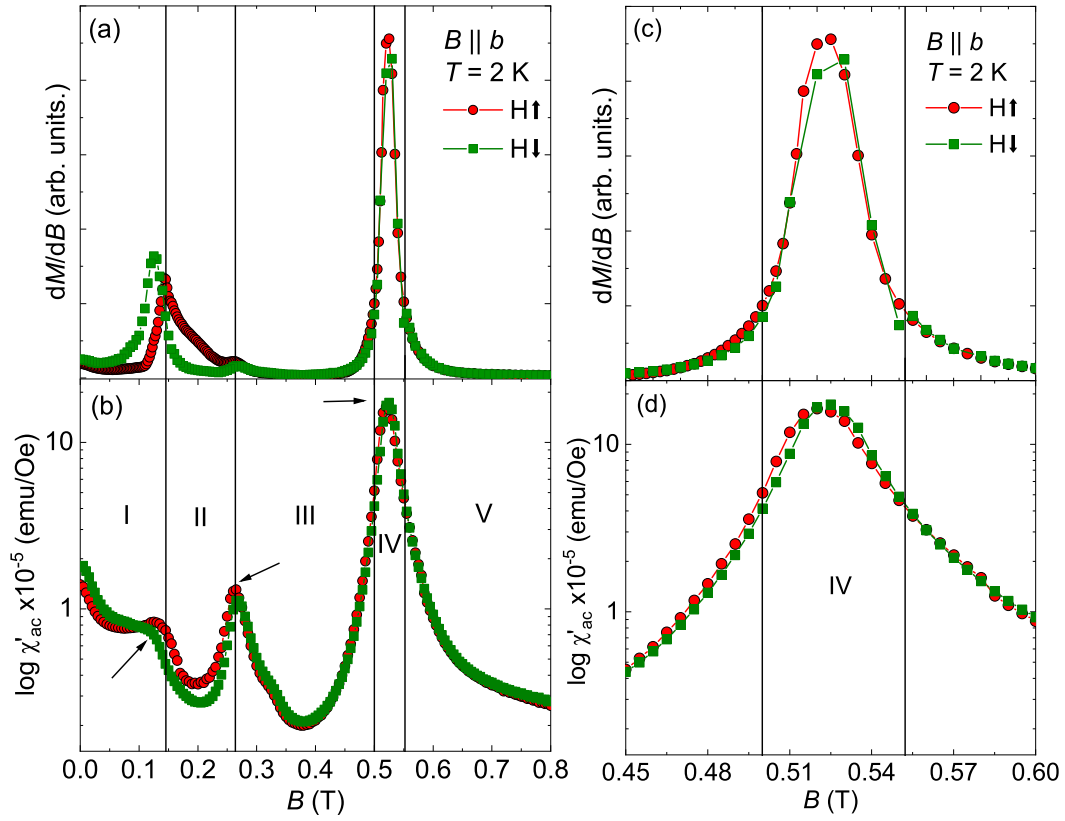


FIG. S4. (a,b) Magnetic field dependence of differential susceptibility (dM/dB) and χ'_{ac} for both up and down sweep cycles at 2 K. The arrow marks indicates positions of B_1 , B_2 , and B_3 similar to Fig. S3. (c,d) Enlarged plots of χ'_{ac} and dM/dB in phase IV regime where a broad nature has been observed.

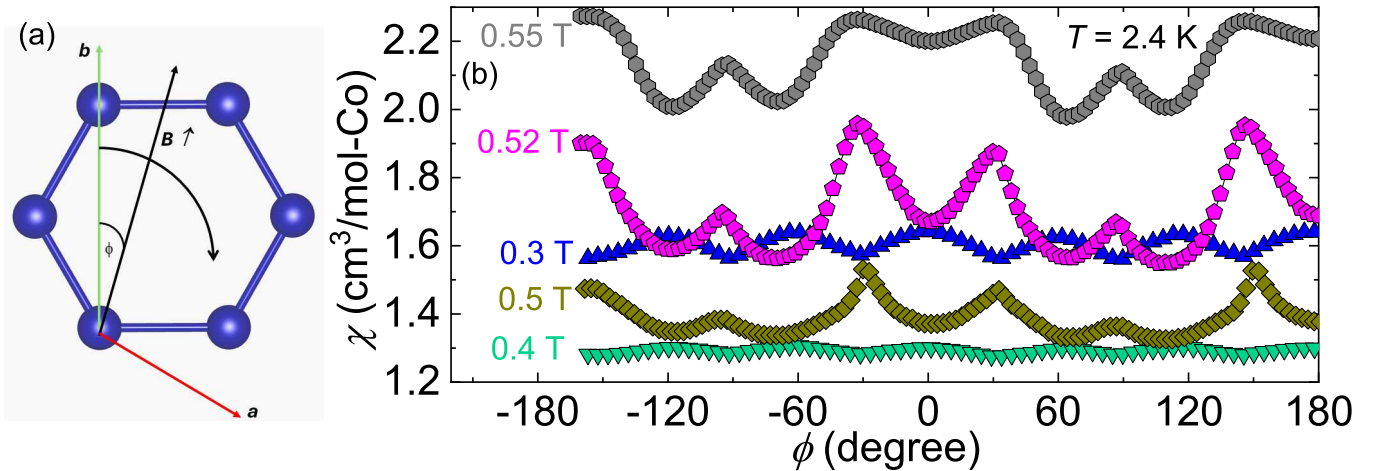


FIG. S5. (a) Definition of the rotation angle ϕ used for the angle-dependent susceptibility. (b) Linear plots of angle-dependent magnetic susceptibility at different fields. The clear exchange between the minima and maxima is seen on going between phases III and IV.

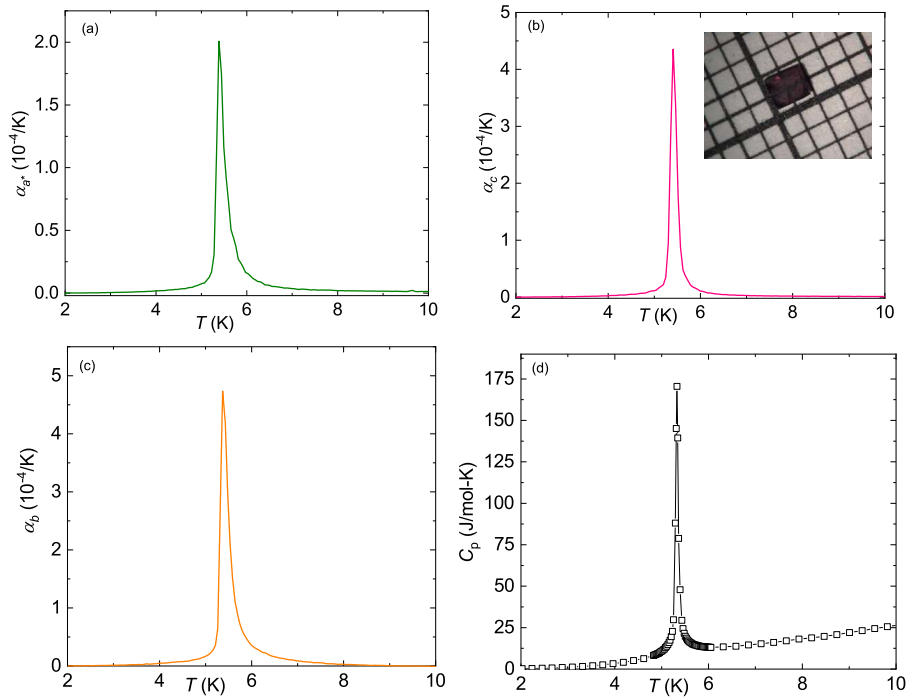


FIG. S6. (a,b,c) Plots of the linear TE coefficient α vs. T for the three crystallographic directions. (b) Zero-field specific heat vs. T for $2 \text{ K} \leq T \leq 10 \text{ K}$.

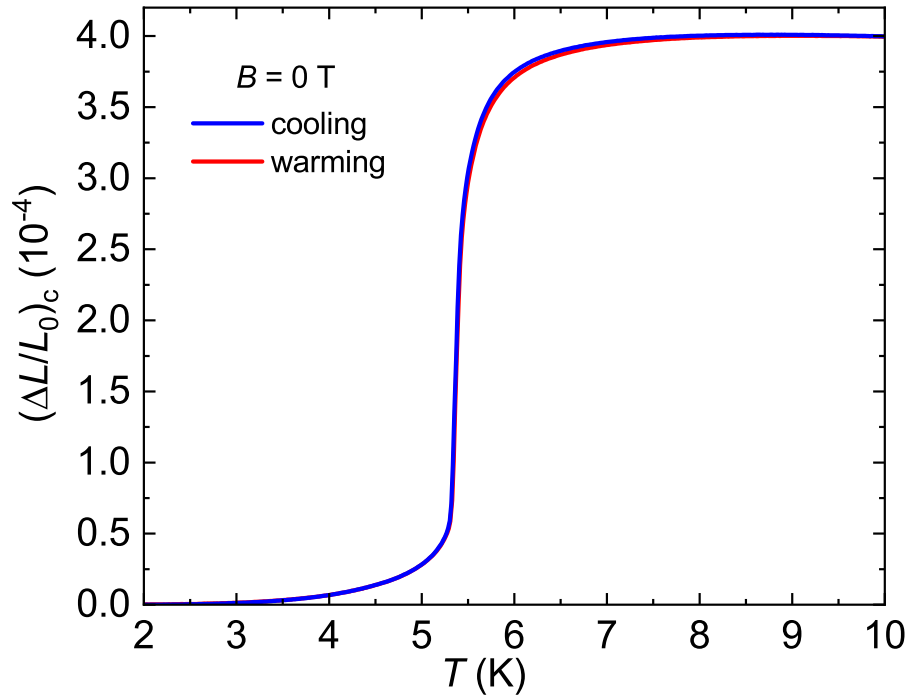


FIG. S7. Relative length change measured at zero magnetic field on cooling and warming shows reversibility and indicates second-order nature of the phase transition in zero field. No anomalies were observed above 10 K up to 300 K.

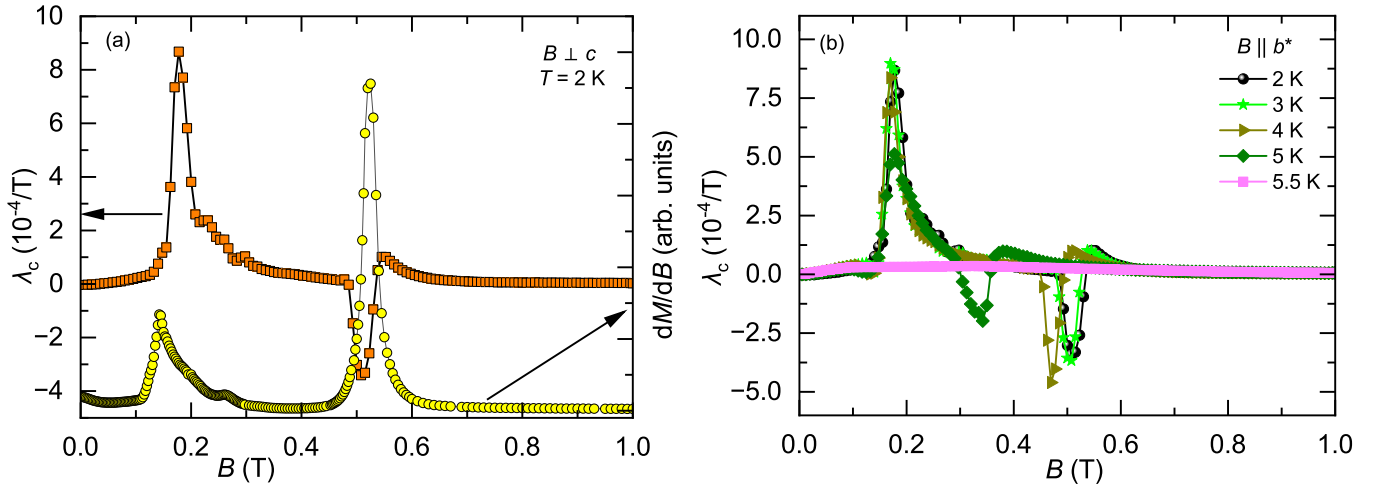


FIG. S8. (a) Magnetic field dependence of λ_c and dM/dB plotted in left and right y -axes respectively at $T = 2\text{ K}$ for the sweep up field cycle. (b) Plots of λ_c vs. B measured up to 1 T for $5.5\text{ K} \leq T \leq 2\text{ K}$.

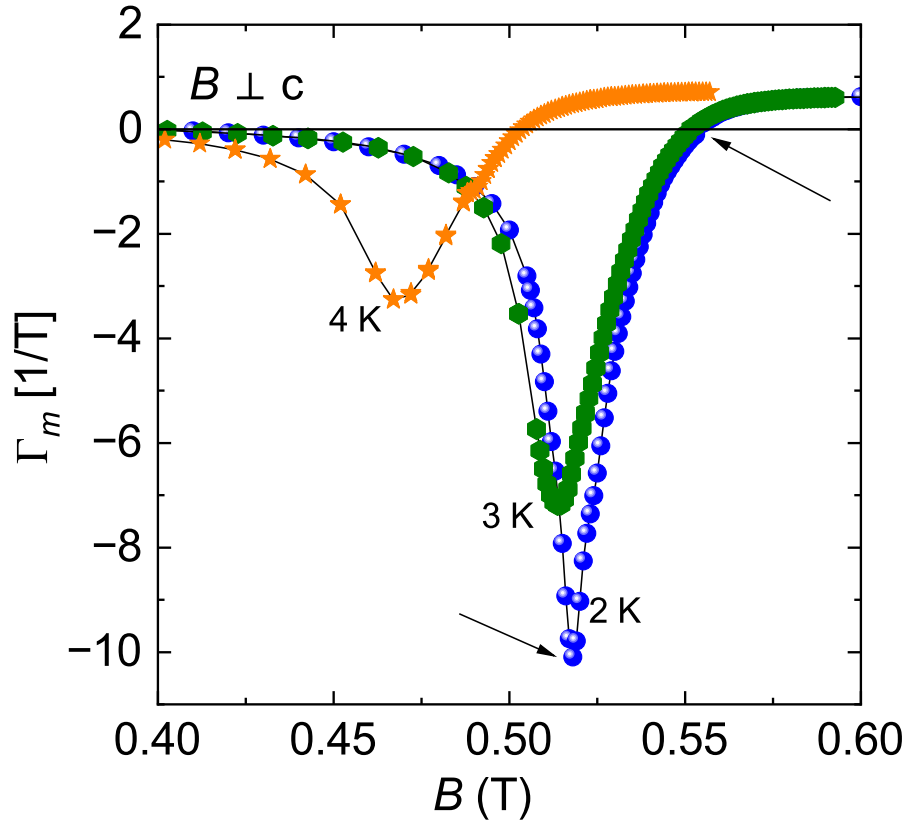


FIG. S9. Magnetic field dependence of the magnetic Grüneissen parameter in phase IV. The two transitions associated with phase IV can be identified from the peak and zero crossing of the Γ_m plots at each temperatures.

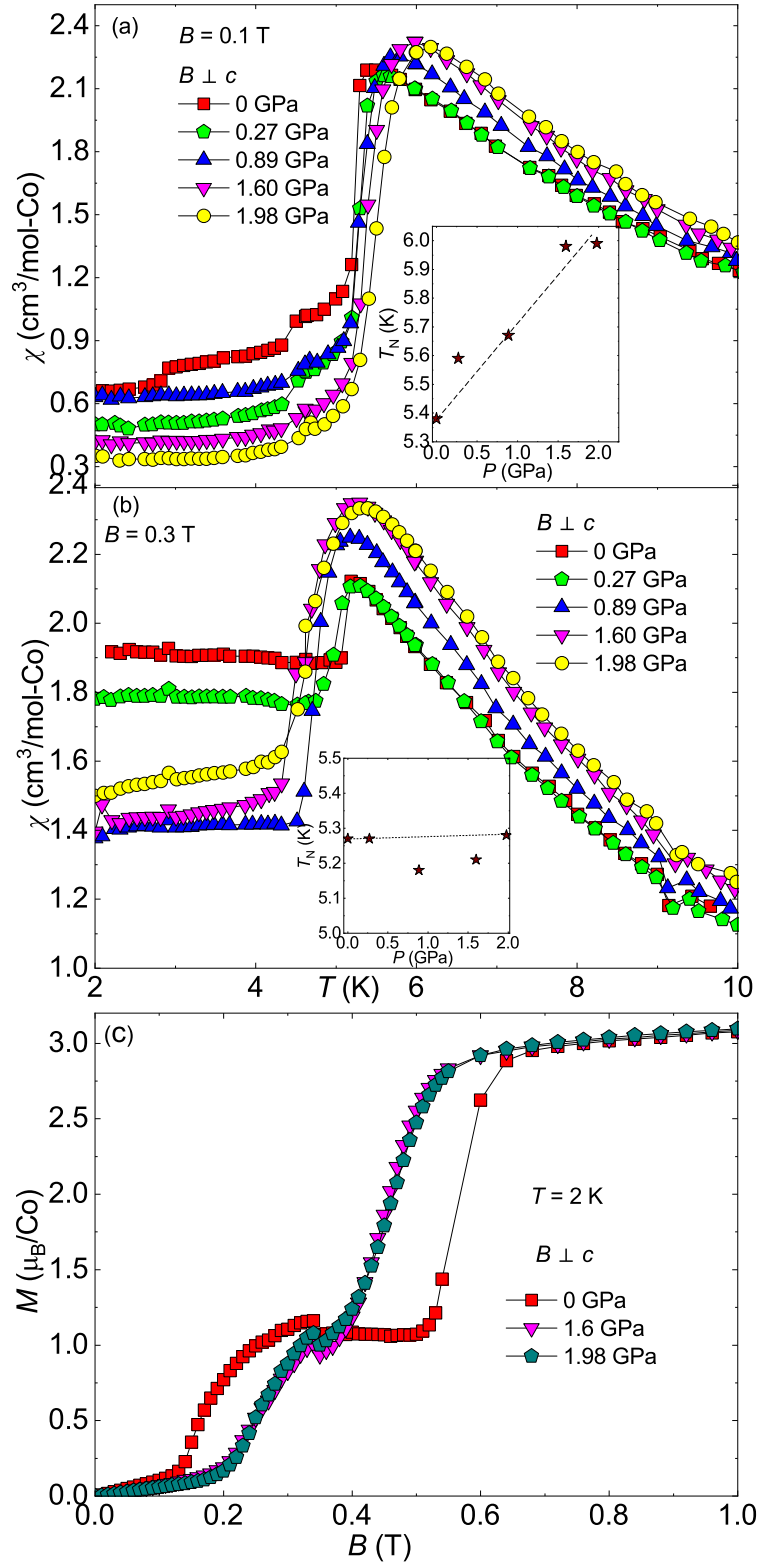


FIG. S10. (a,b) Temperature-dependent DC magnetic susceptibility $\chi(T)$ measured under different pressures from 2 to 10 K under 0.1 and 0.3 T fields. Inset: Corresponding pressure-temperature phase diagram. (c) Magnetic isotherms measured up to 1 T at 2 K for different applied pressures.

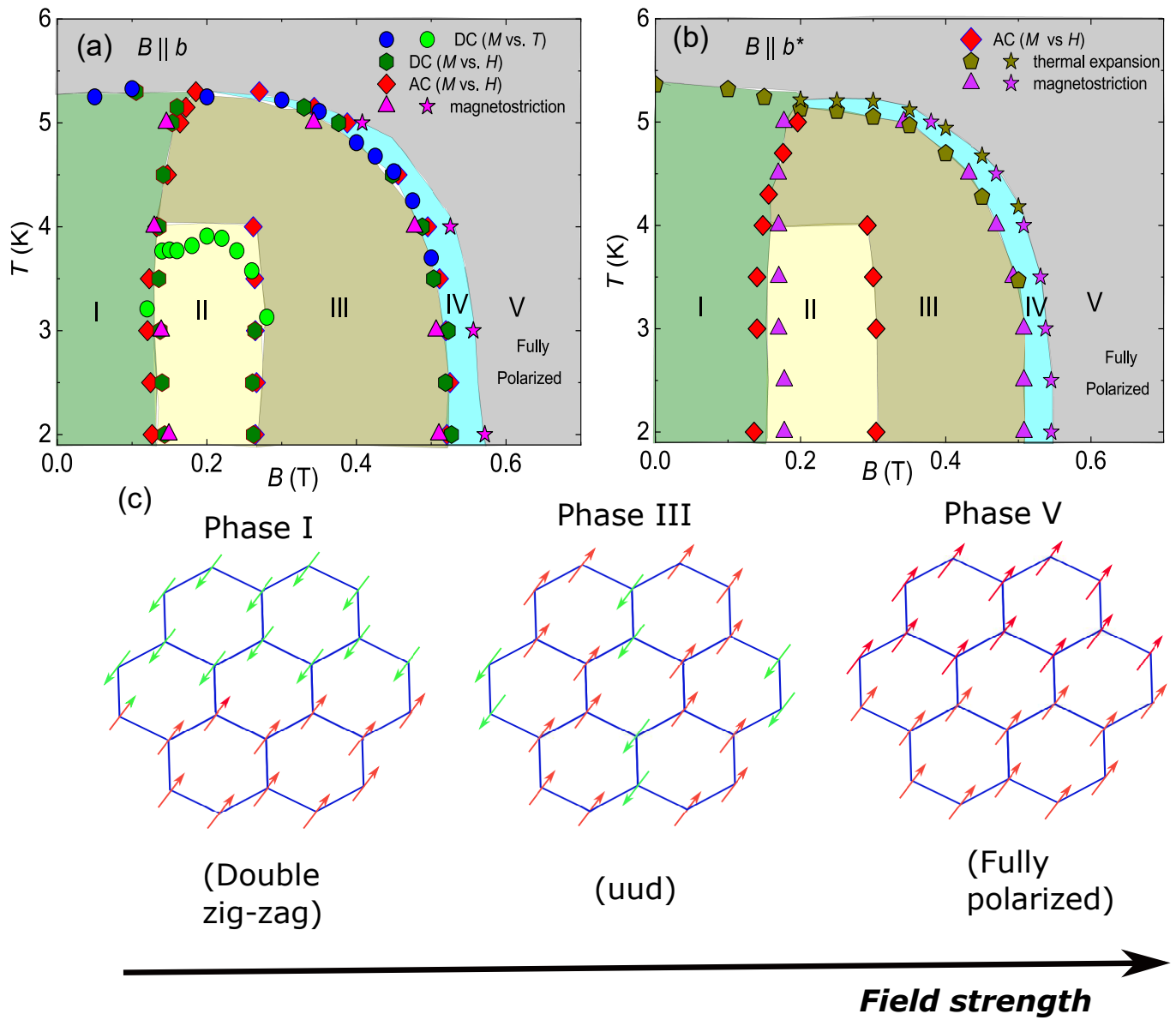


FIG. S11. (a,b) Field-temperature phase diagrams of BCO constructed from the magnetometry and dilatometry measurements, respectively. (c) Schematic presentation of phases I, III, and V in BCO.